Supplementary Material: Mapping astrogliosis in the individual human brain using multidimensional MRI

Dan Benjamini[a,b,c,*], David S Priemer[d,e,f], Daniel P Perl[d,e], David L Brody[c,g,h], Peter J Basser[a,c]

[a] *Section on Quantitative Imaging and Tissue Sciences,Eunice Kennedy Shriver National Institute of Child Health and Human Development, NIH, Bethesda, MD, USA*
[b] *Multiscale Imaging and Integrative Biophysics Unit, Laboratory of Behavioral Neuroscience, National Institute on Aging, NIH, Baltimore, MD, USA*
[c] *Center for Neuroscience and Regenerative Medicine, Uniformed Services University of the Health Sciences, Bethesda, MD, USA*
[d] *Department of Pathology, F. Edward Hébert School of Medicine, Uniformed Services University, Bethesda, MD, USA*
[e] *The Department of Defense/Uniformed Services University Brain Tissue Repository, Bethesda, MD, USA*
[f] *The Henry M. Jackson Foundation for the Advancement of Military Medicine (HJF), Bethesda, MD, USA*
[g] *Department of Neurology, F. Edward Hébert School of Medicine, Uniformed Services University, Bethesda, MD, USA*
[h] *Laboratory of Functional and Molecular Imaging, National Institute of Neurological Disorders and Stroke, NIH, Bethesda, MD, USA*

Supplementary Methods

MRI acquisition

The acquisition of multidimensional data was done using echo planar imaging (EPI) readout according to the MADCO framework encoding scheme [2, 3], and by varying the following three experimental parameters: the inversion time, τ_1, the echo time, τ_2, and the diffusion weighting, b, providing T_1-, T_2-, and diffusion-weighting, respectively.

The minimal values of the two timing parameters, τ_1 and τ_2, depend on the sample physical dimensions because of the varying imaging matrix size that is intended to keep the spatial resolution constant at 200 μm in-plane and 300 μm slice thickness. We kept the minimal τ_1 and τ_2 relatively constant across the samples at $\tau_1 = 12.0 \pm 1.5$ and $\tau_2 = 10.5 \pm 0.8$, by adjusting the number of EPI segments as necessary (<8).

The three 1D distributions of T_1, T_2, and MD, were estimated, respectively, with the following data acquisition protocols: A 1D T_1-weighted data set ($b = 0$, $\tau_2 = 10.5$ ms) with 20 logarithmically sampled τ_1 values ranging from 12 to 980 ms by using an IR-DWI-EPI sequence; a 1D T_2-weighted data set (b=0) with 20 logarithmically sampled τ_2 values ranging from 10.5 to 125 ms by using a DWI-EPI sequence. For diffusion encoding, we used the isotropic generalized diffusion tensor MRI (IGDTI) acquisition protocol to achieve an efficient orientationally averaged DW signal [1] with the following parameters: 16 linearly sampled b-values ranging from 2,540 to 14,700 s/mm^2 in 3 directions, 14 linearly sampled b-values ranging from 4,140 to 14,700 s/mm^2 in 4 directions, and 9 linearly sampled b-values ranging from 8,260 to 14,700 s/mm^2 in 6 directions, using the efficient gradient sampling schemes in Table 2 in [1]. This type of diffusion encoding increases the contrast given by local anisotropy and is not intended to measure the isotropic diffusion in the system. Additional diffusion parameters were gradient duration of $\delta = 4$ ms and diffusion time of $\Delta = 15$ ms.

The three 2D distributions of MD-T_1, MD-T_2, and T_1-T_2, were estimated, respectively, with the following data acquisition protocols (in conjunction with the *a priori* obtained 1D distributions as constraints): A 2D diffusion-T_1-weighted data set with 16 sampled combinations of inversion times and b-values within the aforementioned 1D acquisition range; a 2D D-T_2-weighted data set with 16 sampled combinations of echo times and b-values within the aforementioned 1D acquisition range; and a 2D T_1-T_2-weighted data set with 16 sampled combinations of inversion and echo times within the aforementioned 1D acquisition range.

The data were averaged 4 times to maintain high signal-to-noise ratio (SNR), which was always maintained above 100 (defined as the ratio between the average unattenuated signal intensity within a tissue region of interest, and the standard deviation of the signal intensity within the background). The sample temperature was set at 16.8°C.

Immunohistochemistry

Primary antibodies used were antiglial fibrillary acidic protein (GFAP, mouse antihuman monoclonal antibody GA5 with bond heat-induced epitope retrieval, epitope retrieval time 10 minutes, PA0026; Leica Biosystems, Wetzlar, Germany), amyloid precursor protein (APP, mouse antihuman monoclonal antibody clone 22c11, dilution 1:10, epitope retrieval time 10 minutes, MAB348; EMD Millipore, Burlington, MA), and abnormally phosphorylated tau (AT8; mouse anti-human monoclonal antibody, dilution 1:2000, Thermo Scientific, MN1020, HIER 1:10 for 10 min), and myelin basic protein (MBP, 1:100, epitope retrieval time 10 minutes, ab62631; Abcam, Cambridge, MA).

*Corresponding author. Phone: +1-667-312-3569
Email address: dan.benjamini@nih.gov (Dan Benjamini)

Statistical analysis

A linear mixed-effects model was evaluated using the mean ROI values for MD-T_1, MD-T_2, and T_1-T_2, AD, RD, FA, T_1 or T_2 as the dependent variable and GFAP histological density and age as the independent variables. A random intercept for each subject was included. Within subjects, the different ROIs are derived from the same image and therefore cannot be assumed to be independent. Similarly, the noise cannot be modeled as identical and independent within subjects. To address that, we included a Gaussian structured noise covariance matrix in the model to account for spatial correlation among ROIs. In this case, the noise covariance between two voxels separated by distance d is proportional to a Gaussian parametric function, $exp(-(r/d)^2)$, where r is a parameter to be estimated.

Supplementary Results

Anomaly detection algorithm on voxel-averaged maps

We applied an adjusted anomaly detection machine learning algorithm on conventional maps to make a valid comparison between 1D voxel-averaged T_1, T_2, AD, RD, and FA maps versus the newly generated multidimensional maps for detecting astrogliosis. The same initial steps in the original processing procedure (Fig. 4 A-E) were used here. The cross-validation steps, however, could not be performed in the exact same fashion because of the inherent difference between scalar values and distributions. Once all normal-appearing voxels are identified within a subject, a Monte Carlo cross-validation procedure is used to create multiple random splits ($N_{cv} = 1000$ in this study) of 66% and 34% of the normal-appearing voxels into training and validation data, respectively. For each such split, instead of obtaining the normative spectral signature (e.g., T_1-MD) and then train to find deviations from it, in the case of voxel-averaged data we first save a list of the normative scalar values using the 'normal' tissue image mask. The next step determines the range of normative scalar values for a particular subject; we tested two ranges, $\mu \pm \sigma$ and $\mu \pm 2\sigma$, where μ and σ represent the mean and standard deviation of the normative values, respectively. By applying the same logic as in the multidimensional anomaly detection algorithm, knowing the range of normative voxel-averaged values allows to find the voxels that reside outside of this range, and subsequently label them as abnormal regions. It is now clear that the $\mu \pm 2\sigma$ range is more conservative by design than the $\mu \pm \sigma$ range because it allows for less 'abnormal' voxels. This process is repeated $N_{cv} = 1000$ times to allow the assessment of uncertainty and predictive accuracy, resulting in a set of 'abnormal' range values per subject. The minimal value of $\mu - \sigma$ (or $\mu - 2\sigma$) and maximal value of $\mu + \sigma$ (or $\mu + 2\sigma$) across all splits is selected, and used to produce final binary maps of abnormal regions (shown in Fig. S6).

Using these final binary maps of abnormal regions as masks on their respective adjusted T_1, T_2, AD, RD, and FA maps results in corresponding 'abnormal' maps. We show these maps along with histological GFAP density images of six representative control (Cases 3, 4, and 7) and injured cases (Cases 10, 11, and 12) shown in Figs. S7 and S8 using the $\mu \pm \sigma$ and $\mu \pm 2\sigma$ normative ranges, respectively.

The non-specificity of these so-called abnormal regions is clear. The less conservative normative range of $\mu \pm \sigma$ resulted in inconsistent labeling across the different subjects, even within a particular voxel-averaged metric. For instance, the final binary maps of abnormal regions from voxel-averaged T_1 indicated that astrogliosis is abundant in the control cases (Figs. S6-S7, A-C), with presence in most of the WM (Case 3), in all of the GM (Case 4), and both WM and GM (Case 7). The specificity towards astrogliosis did not improve in the injured subjects (Figs. S6-S7, D-F), where in cases 10 and 11 all of the WM deemed abnormal, and an inconsistent mixture of GM and WM in Case 12 was found to contain astrogliosis. To improve the specificity, the more conservative normative range of $\mu \pm 2\sigma$ was used as well. However, in most instances, it resulted in very scattered detection that did not to agree with the underlying anatomy and pathology of the tissue (Fig. S8).

The clear lack of similarity and agreement between the MRI maps and GFAP histology in Figs. S7 and S8 shows that despite using an anomaly detection machine learning algorithm, the microstructural and chemical composition changes induced by astrogliosis are still averaged-out when one only considers scalar value MRI maps.

Supplementary Table and Figures

Table S1: **Medical and neuropsychiatric history in subjects with history of traumatic brain injury (TBI) and healthy controls**

Case	Medical history	Neuropsychiatric history
1	Hyperlipidemia, sleep apnea, shingles, retinal tear	None reported
2	Alcohol abuse, diabetes	Depression
3	Diabetes, myocardial infarction, essential thrombocytosis	None reported
4	Hypertension, congestive heart failure, aortic valve replacement,diabetes, COPD	None reported
5	Sports injuries: torn retina, torn patellar tendon, torn ACL	None reported
6	Alcohol abuse	None reported
7	Diabetes, hypertension, hypercholesterolemia	None reported
8	Soft tissue injury, chronic pain	PTSD, reduced cognitive function, confusion, memory loss, seizures, paranoia, delusions, emotional liability
9	Soft tissue injury, chronic pain, low testosterone, alcohol abuse	PTSD, anxiety, depression
10	Alcohol and polysubstance abuse, chronic pain, urinary tract infection	PTSD, anxiety, depression
11	Cannabis abuse, alcohol abuse, low testosterone	PTSD, unspecified bipolar/paranoid disorder
12	None reported	Sleep disturbance, anxiety, depression
13	Hypertension, hyperlipidemia, coronary artery disease	None reported
14	None reported	PTSD, anxiety, depression

Chronic obstructive pulmonary disease (COPD), Anterior cruciate ligament (ACL), Post traumatic stress disorder (PTSD)

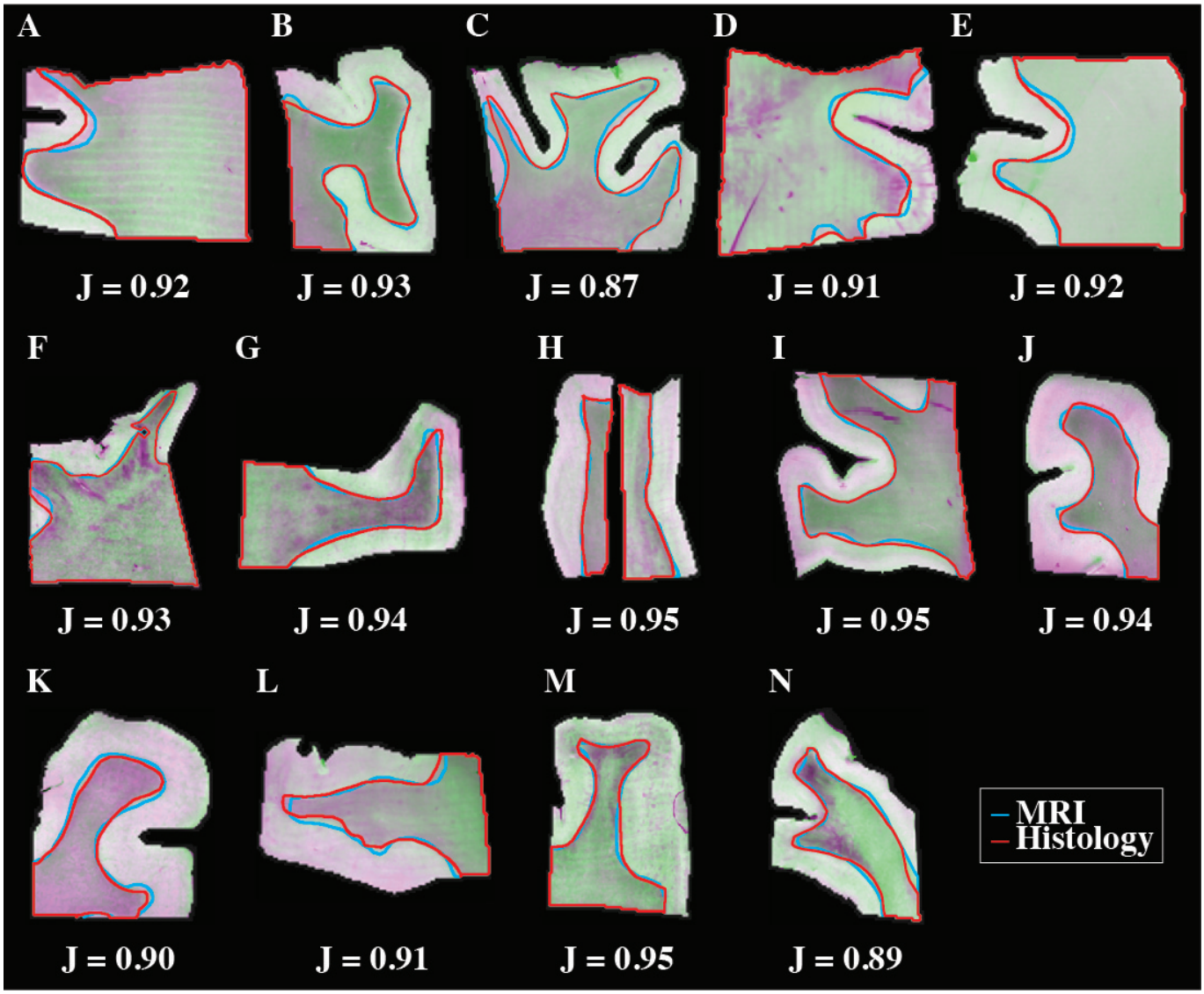

Figure S1: MRI and histopathology co-registration qualitative and quantitative accuracy assessments. The transformed histology images were overlaid on MR images using independent intensity scales (purple for GFAP and green for MRI) to assess the quality of the co-registration. The Jaccard index, J, was computed to quantify the overlap scores between the co-registered modalities. In addition, qualitative agreement is demonstrated by the overlap in WM-GM interfaces of the MRI and GFAP histology images, which are shown in blue and red, respectively.

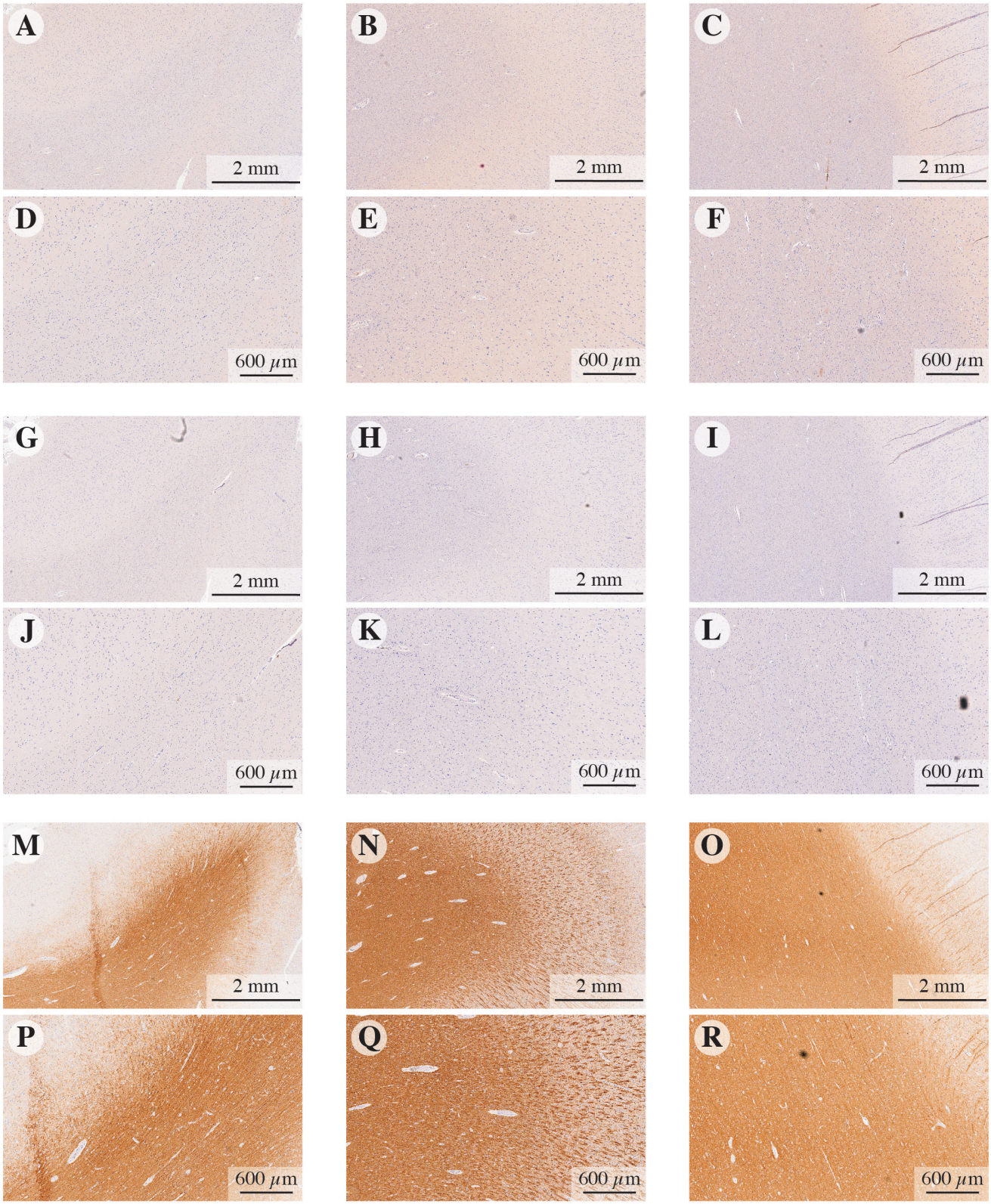

Figure S2: Amyloid precursor protein (APP), phosphorylated tau (pTau), and myelin basic protein (MBP) immunoreactivity in representative cases. Subject with impact TBI but without blast exposure (Case 3): (A) and (D) show APP, (G) and (J) show pTau, and (M) and (P) show MBP. Subject without impact TBI but with blast exposure (Case 11): (B) and (E) show APP, (H) and (K) show pTau, and (N) and (Q) show MBP. Subject with both impact and blast exposure TBI (Case 8):(C) and (F) show APP, (I) and (L) show pTau, and (O) and (R) show MBP. No axonal damage (APP), tau pathology (pTau), or demyelination (MBP) were observed in any other the cases in this study.

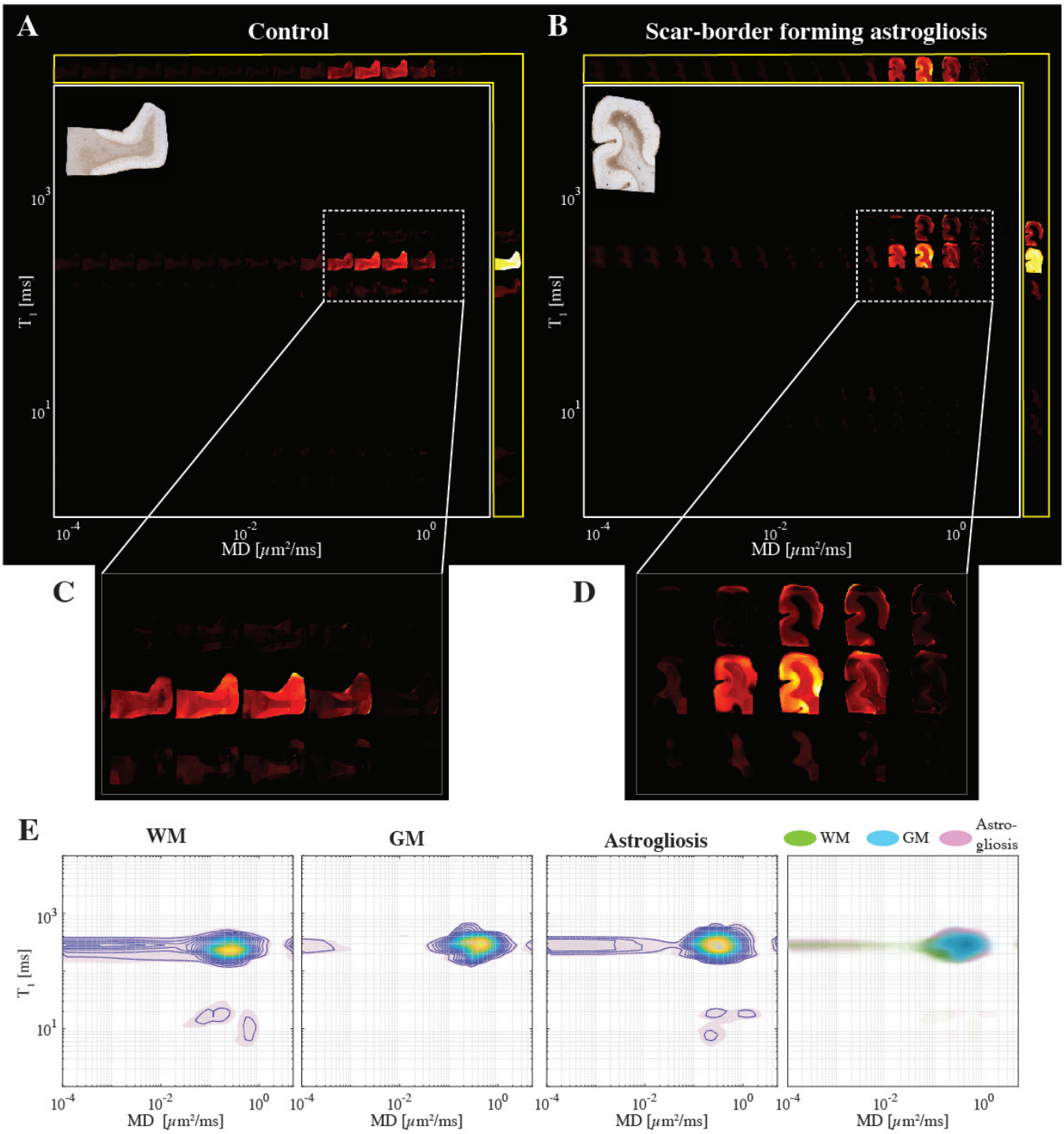

Figure S3: Changes in the T_1-MD multidimensional MR signature induced by confirmed astrogliosis. Maps of 2D spectra of subvoxel T_1-MD values reconstructed on a 16×16 grid of a representative (A) control (case 7) and (B) injured (case 10) subjects, along with their respective GFAP histological image (top left of each panel). Magnified spectral regions showing highest content of spectral information from (C) control and (D) injured cases. (E) T_1-MD spectra averaged across all subjects in WM, GM, and GFAP-positive regions of interest (ROIs, left to right), and a superposition of the average spectra from the three ROIs.The Jensen Distances between the regions with astrogliosis and normal-appearing WM, and between regions with astrogliosis and normal-appearing GM T_1-MD spectral signatures were 0.07 and 0.08, respectively. The Jensen Distances between normal-appearing WM and GM was 0.13.

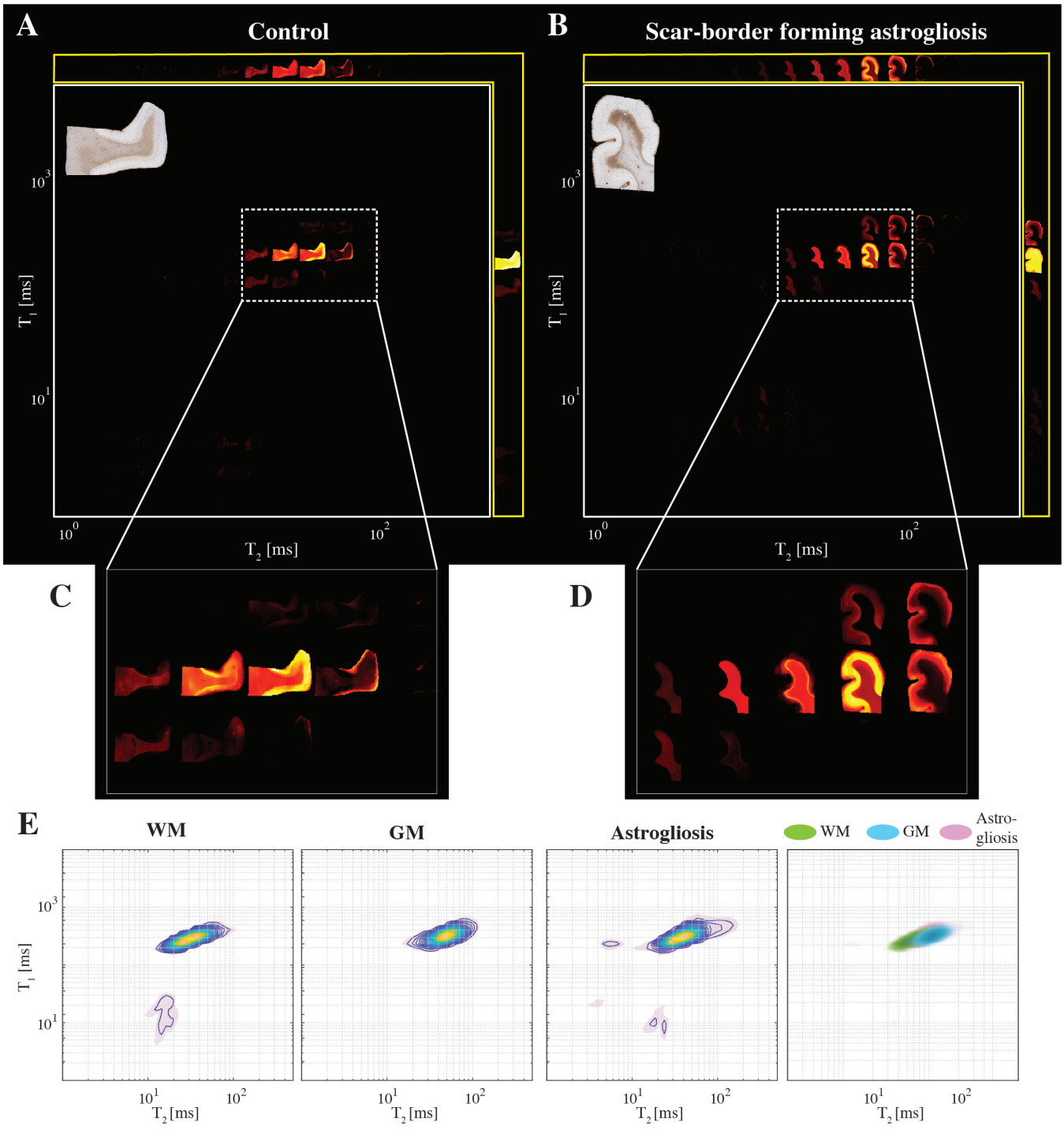

Figure S4: Changes in the T_1-T_2 multidimensional MR signature induced by confirmed astrogliosis. Maps of 2D spectra of subvoxel T_1-T_2 values reconstructed on a 16×16 grid of a representative (A) control (case 7) and (B) injured (case 10) subjects, along with their respective GFAP histological image (top left of each panel). Magnified spectral regions showing highest content of spectral information from (C) control and (D) injured cases. (E) T_1-T_2 spectra averaged across all subjects in WM, GM, and GFAP-positive regions of interest (ROIs, left to right), and a superposition of the average spectra from the three ROIs. The Jensen Distances between the regions with astrogliosis and normal-appearing WM, and between regions with astrogliosis and normal-appearing GM T_1-T_2 spectral signatures were 0.09 and 0.11, respectively. The Jensen Distances between normal-appearing WM and GM was 0.21.

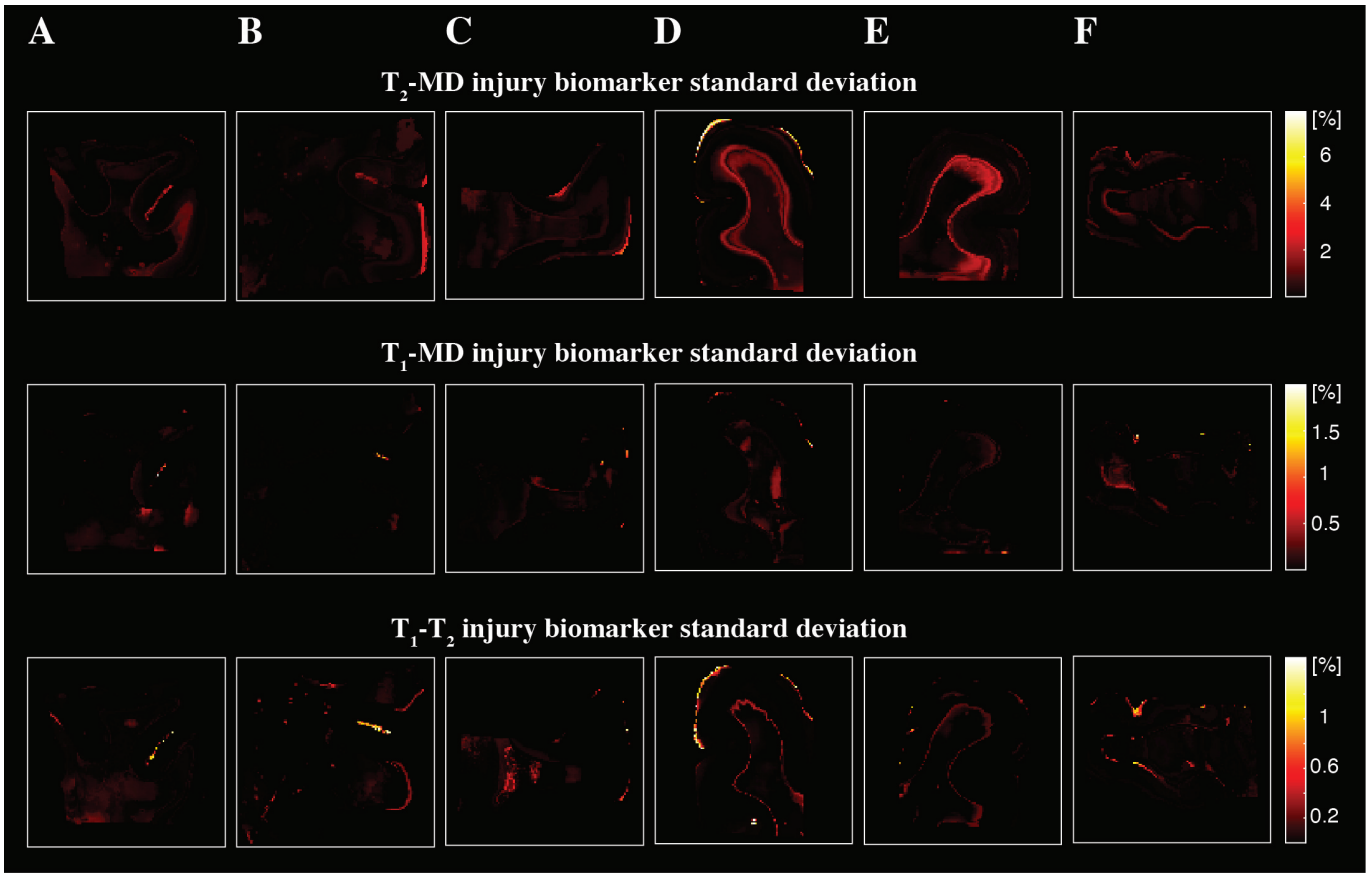

Figure S5: Maps of injury biomarkers standard deviations from the cases in Fig. 5. The standard deviations were computed from the Monte Carlo cross-validation procedure for anomaly detection in individuals. (A)-(C) are subjects that were not exposed to blast (Cases 3, 4, and 7), while (D)-(F) were (Cases 10-12). The standard deviations are under an order of magnitude smaller than the corresponding means, pointing to relative stability and low uncertainty.

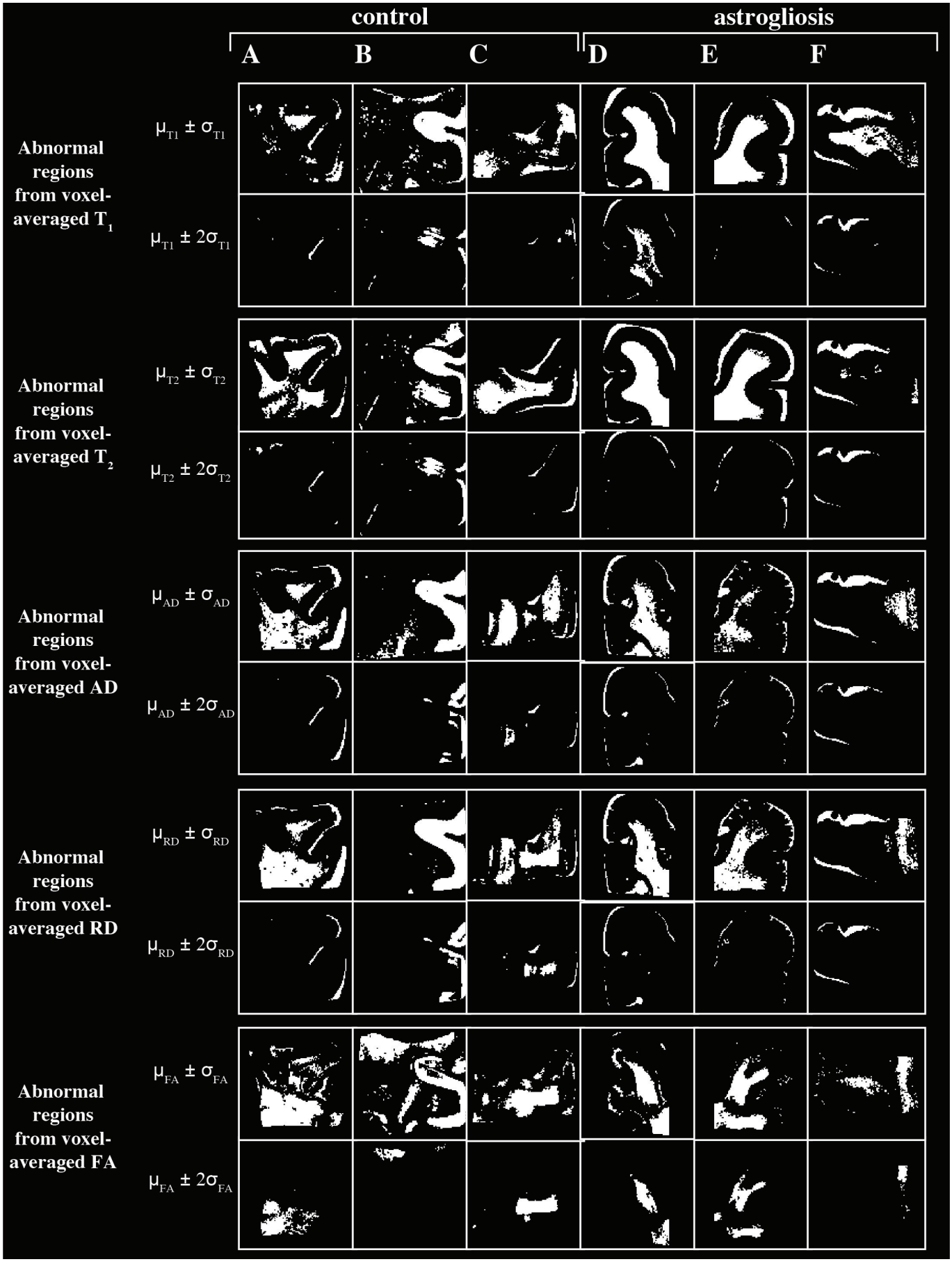

Figure S6: Final binary maps of suspected abnormal regions based on 1D voxel-averaged data. Six representative cases are shown. (A)-(C) are subjects without severe astrogliosis (Cases 3, 4, and 7), while (D)-(F) had substantial GFAP over-expression (Cases 10-12). Two thresholds for values that are considered within the normative range were used: $\mu \pm \sigma$ and $\mu \pm 2\sigma$, resulting in less and more conservative injury detection, respectively. Note the clear lack of similarity and agreement between these MRI maps GFAP histology (shown in, e.g., Fig. S6).

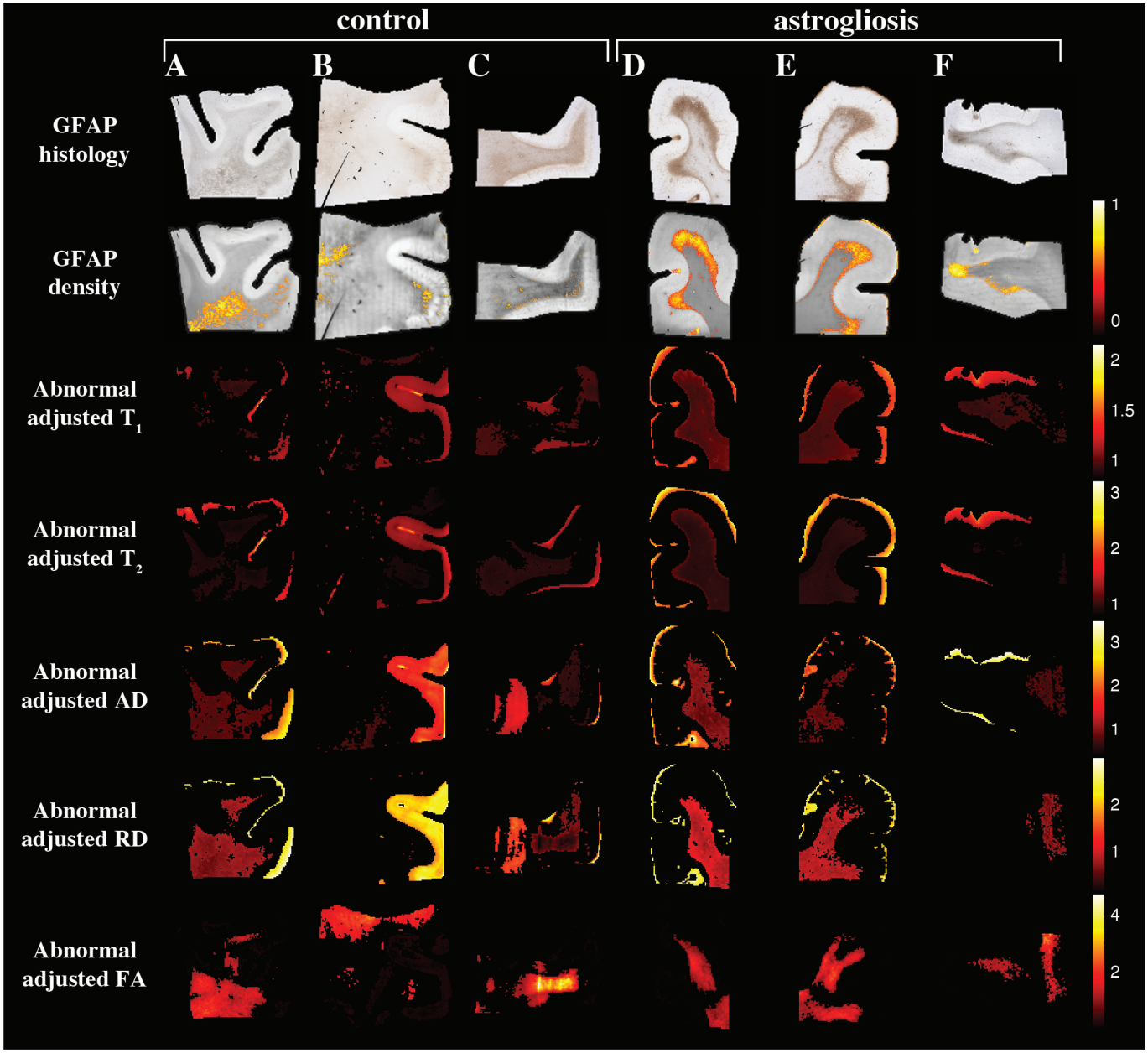

Figure S7: Voxel-averaged MRI maps obtained using the anomaly detection algorithm with $\mu \pm \sigma$. (A)-(C) are subjects without severe astrogliosis (Cases 3, 4, and 7), while (D)-(F) had substantial GFAP over-expression (Cases 10-12). The different rows correspond to the different MRI contrasts, including all the conventional relaxation and DTI parameters. In addition, the co-registered histological GFAP images and density maps are shown. The abnormal regions in these T_1, T_2, AD, RD, and FA maps do not correspond to the histological ground truth, and lack specificity towards astrogliosis.

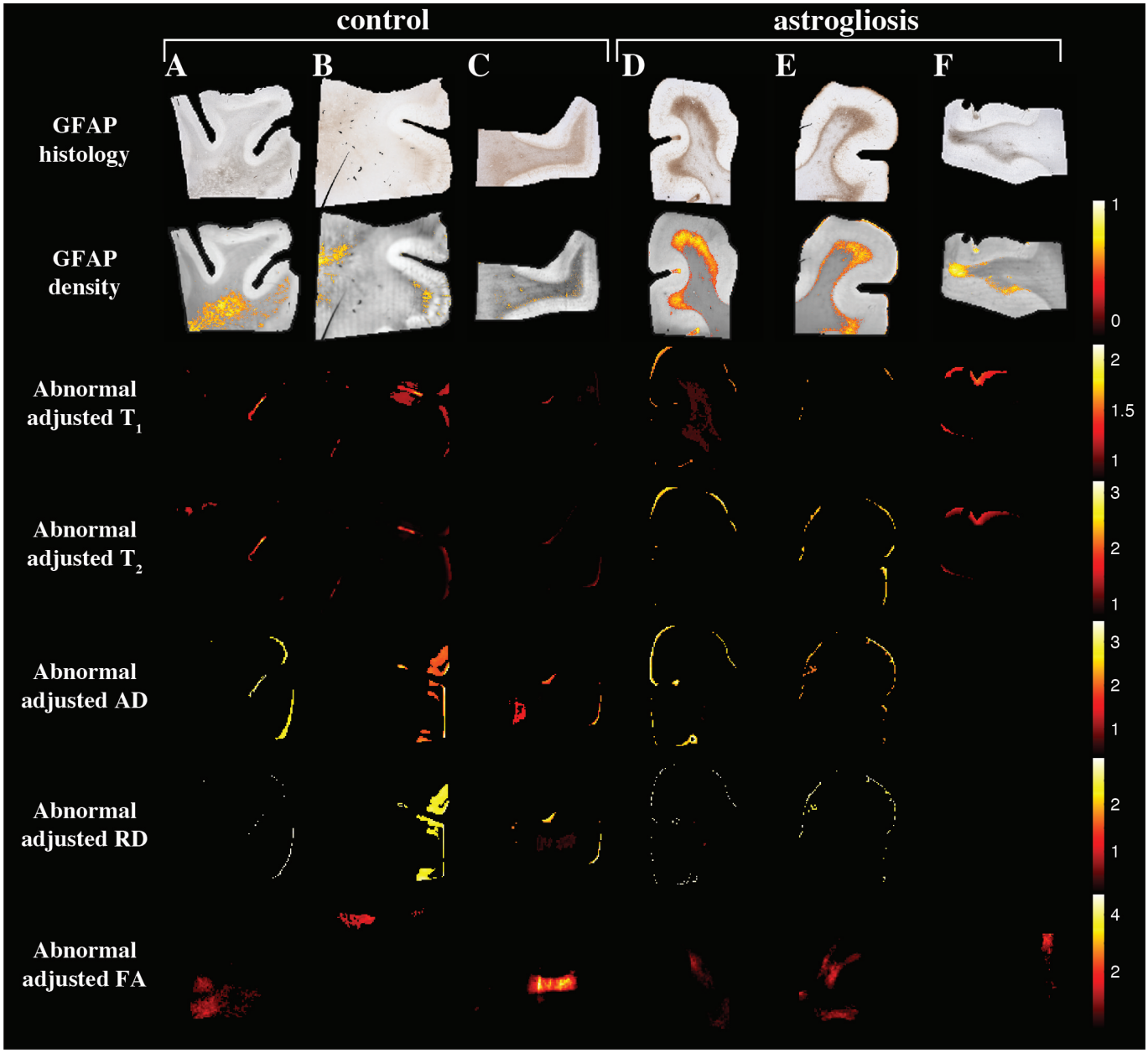

Figure S8: Voxel-averaged MRI maps obtained using the anomaly detection algorithm with $\mu \pm 2\sigma$. (A)-(C) are subjects without severe astrogliosis (Cases 3, 4, and 7), while (D)-(F) had substantial GFAP over-expression (Cases 10-12). The different rows correspond to the different MRI contrasts, including all the conventional relaxation and DTI parameters. In addition, the co-registered histological GFAP images and density maps are shown. The abnormal regions in these T_1, T_2, AD, RD, and FA maps do not correspond to the histological ground truth, and lack specificity towards astrogliosis.

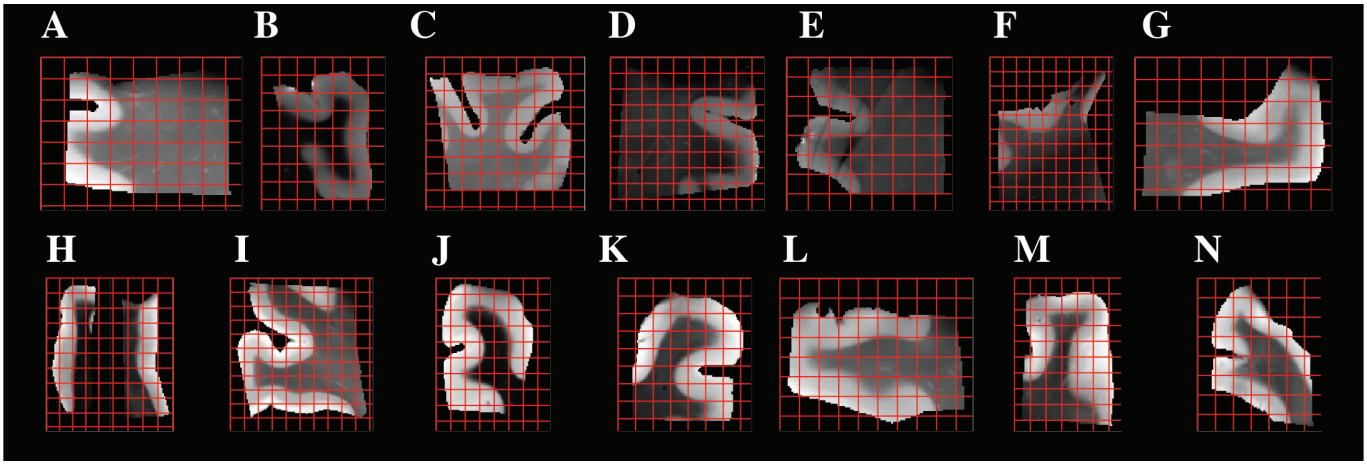

Figure S9: Downsampled MR images from all cases, used for whole image correlation. After matching the GFAP density images resolution to their MRI counterparts, both MRI and histological maps were downsampled by a factor of 12 to account for co-registration errors and to reduce spatial dependencies, resulting in a total of 556 pairs of MR image volumes and GFAP densities from all 14 subjects.

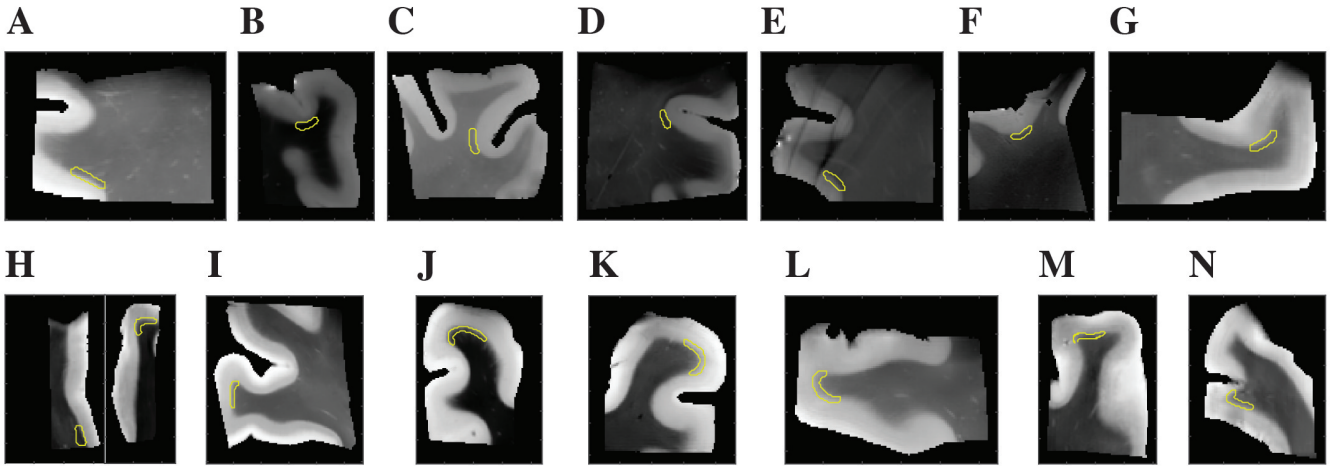

Figure S10: Gray-white matter interface regions of interest shown on proton density MR images.

References

[1] Avram, A.V., Sarlls, J.E., Hutchinson, E., Basser, P.J., 2018. Efficient experimental designs for isotropic generalized diffusion tensor MRI (IGDTI). Magnetic Resonance in Medicine 79, 180–194.

[2] Benjamini, D., Basser, P., 2016. Use of marginal distributions constrained optimization (madco) for accelerated 2d mri relaxometry and diffusometry. Journal of Magnetic Resonance 271, 40–45. doi:10.1016/j.jmr.2016.08.004.

[3] Benjamini, D., Iacono, D., Komlosh, M.E., Perl, D.P., Brody, D.L., Basser, P.J., 2021. Diffuse axonal injury has a characteristic multidimensional mri signature in the human brain. Brain 144, 800–816. doi:10.1093/brain/awaa447.